ANNALS OF GEOPHYSICS, 66, 2, SE209, 2023; doi:10.4401/ag-8829
OPEN ACCESS

Shear-wave splitting patterns in Perachora (Eastern Gulf of Corinth, Greece)

Ioannis Spingos*[,1], Vasilis Kapetanidis[1], Georgios Michas[1], George Kaviris[1], Filippos Vallianatos[1,2]

(1) Section of Geophysics - Geothermics, Department of Geology and Geoenvironment, National and Kapodistrian University of Athens, Athens, Greece
(2) Institute of Physics of Earth's Interior and Geohazards, UNESCO Chair on Solid Earth Physics and Geohazards Risk Reduction, Hellenic Mediterranean University Research Center, Crete, Greece

Article history: received April 1, 2022; accepted October 1, 2022

Abstract

The Eastern Gulf of Corinth (EGoC) is one of the most seismically active areas in Greece. It is monitored by local and regional seismic stations of the Hellenic Unified Seismic Network (HUSN). In 2020, a high-yield seismic sequence, lasting over five months, occurred at the Perachora peninsula. This provided a unique opportunity to investigate the anisotropic properties of the upper crust in the area, which lacks relevant studies. The sequence exhibited characteristics of a seismic swarm, with the strongest event having a magnitude of 3.7. In the herein analysis, we use recordings from suitable HUSN stations for two periods: (a) 2008 to 2019, a period of scarce seismicity, to identify background anisotropy and (b) the 2020 seismic swarm period. We used a fully automated method to measure shear-wave splitting properties. After considering a shear-wave window of 45° and several quality criteria, we determined a complex state of anisotropy, with NE-SW directions of polarization (φ) prevailing pre-2020, while a dominant WNW-ESE orientation was observed during the swarm (with secondary NE-SW and N-S trends). The spatial distribution of φ did not offer any strong correlation with local faults. Additionally, φ seemed to rotate in 2015 and 2020, with variations of normalized time-delays being present during the crisis. These observations, along with indications regarding fluid diffusion during the swarm, led us to hypothesize that shear-wave splitting in the EGoC is mainly driven by high pressure gradients. A better understanding of pre-2020 seismicity and more local stations to record future seismicity would be required to further specify the connection between fluid processes and seismic anisotropy in the area.

Keywords: Seismic anisotropy; Shear-wave splitting; Eastern Gulf of Corinth; Microcracks; Anisotropic Poro-Elasticity

1. Introduction

Shear-wave Splitting (SwS) is a phenomenon observed when a shear-wave enters an anisotropic medium and splits, producing two orthogonally polarized waves, propagating with different velocities. SwS is well-established over a wide range of scales; from teleseismic waves travelling through the outer core and mantle [Savage and Silver, 1993; Hatzfeld et al., 2001; Audoine et al., 2004; Evangelidis, 2017; Kaviris et al., 2018a; Chen et al., 2021] to local recordings characterizing the upper crust [Paulssen, 2004; Peng and Ben-Zion, 2004; Li et al., 2015; Johnson and Savage, 2012; Adelinet et al., 2016; Kaviris et al., 2021, 2020, 2018b; Karlowska et al., 2021] and, even, more constrained settings such as mines [Wuestefeld et al., 2011] and laboratory experiments [Gao and Crampin, 2003; Tillotson et al., 2012]. Splitting can be quantified by exploring two fundamental parameters: the polarization angle (φ) of the shear-wave travelling with the higher velocity (S_{fast}) and the time-delay (t_d) of the slower shear-wave's (S_{slow}) arrival.

The mechanisms responsible for SwS can be diverse, based on the scale under investigation. The common denominator is the pervasion of the rock volume that the shear-wave goes through by features of similar geometry. Therefore, splitting can be the result of mantle flow [Abt and Fischer, 2008; Hammond et al., 2010], rock lamination [Valcke et al., 2006], or oriented microcracks [Kaneshima et al., 1988] which is, probably, the most common source of splitting in the upper crust. The latter hosts microscopic cracks and fractures that are filled with fluids, such as meteoric water or hydrocarbons [Crampin and Atkinson, 1985]. Stress can have a significant effect on inherent micro-defects within a rock mass (such as grain boundaries or intracrystalline cavities) and alter the morphology and dynamics of the microcracks [Kranz, 1983]. The Anisotropic Poro-Elasticity (APE) model [Crampin and Zatsepin, 1997; Zatsepin and Crampin, 1997] argues the existence of fluid-saturated microcracks that are closely spaced and, as the stress equilibrium shifts, eventually concatenate to form a larger fracture that leads to an earthquake. The polarization of the S_{fast} is oriented according to the maximum horizontal compressive stress component (σ_{Hmax}), while the time-delay, which accumulates along the ray-path, is affected by crack density. A major component of this model is the effect of fluid flow and diffusion along pressure gradients between cracks, causing orientations that divert from the stress field [Crampin et al., 2004]. APE aimed to explain the physical mechanism that controls the fluid-filled microcracks, earlier described by Extensive-Dilatancy Anisotropy (EDA) [Crampin et al., 1984; Crampin, 1987]. Furthermore, SwS measurements have reportedly been used to “stress-forecast” a $M = 5.0$ earthquake in Iceland [Crampin et al., 1999].

In our study, we investigate SwS in the Eastern Gulf of Corinth (EGoC). Contrary to its western counterpart, where shear-wave splitting, and its relation to local faults and stresses, has been extensively documented [Bouin et al., 1996; Bernard et al., 1997; Giannopoulos et al., 2015; Kaviris et al., 2017; Kaviris et al., 2017, 2018b; Kapetanidis et al., 2021], similar studies in the EGoC are sparse [Papadimitriou et al., 1999; Kaviris, 2003; Kaviris et al., 2014]. This is a direct consequence of the relatively mild seismicity in the area, as well as the availability and geometry of local seismic stations. The EGoC has witnessed the occurrence of strong and destructive earthquakes during both historic and modern times [Makropoulos et al., 2012; Stucchi et al., 2013; Ambraseys, 2015], but only few seismic swarms have been recorded [Mesimeri et al., 2018; Michas et al., 2022]. The strongest events of the past century were the ones that occurred in 1981, since dubbed the Alkyonides earthquakes [Papazachos et al., 1984], which concern a series of $M > 6.0$ shocks during a period of few weeks. These events led to increased interest in the area, as they decimated the region around the nearby town of Loutraki and affected Athens, the capital of Greece [Papanastassiou, 2002]. The roughly WNW-ESE and NW-SE faults, such as Pisia (Figure 1a) and Schinos, have been associated with the 1981 seismicity, with the two being suggested as the causative faults of the first two $M > 6.0$ events [Taymaz et al., 1991; Hubert et al., 1996]. The Pisia fault has witnessed similarly strong earthquakes in the earlier Holocene, with significant slip rates [Mechernich et al., 2018]. Nevertheless, Jackson et al. [1982] located the first event offshore, in an area NW of the Perachora fault. Highly segmented fault systems with a general NW-SE to WNW-ESE and ENE-WSW orientation have been identified [Vita-Finzi and King, 1985], which feature a low earthquake productivity rate [Hatzfeld et al., 2000]. Focal mechanisms in the area (Figure 1a) follow fault geometry and indicate normal kinematics, therefore supporting a general WNW-ESE to NW-SE σ_{Hmax} orientation [Kapetanidis and Kassaras, 2019; Kassaras et al., 2020]. However, there are exceptions of tectonic structures with differing orientations, as in the case of the offshore Perachora (Figure 1a) and Heraion faults [e.g. Michas et al., 2015]. The strong tectonic footprint in the Gulf of Corinth has been a shaping factor for infrastructure and the urban environment since the antiquity [Marriner and Morhange, 2007]. Geologically, the alpine basement of the Perachora peninsula consists of Triassic to Lower Jurassic limestones with an overlying series of volcanic and sedimentary rocks (Upper Jurassic) capped by two flysch deposits, one in the Lower and one in the Upper Cretaceous. Pliocene deep-water marls are overlain by shallower Pleistocene deposits [IGME, 1984].

Generally, seismicity in the broader EGoC has been mild, with few seismic sequences at crustal depths. Since 2008, seismicity around the Perachora peninsula has been sparse, with the largest event of $M_w = 5.1$ (Fig. 1b), located

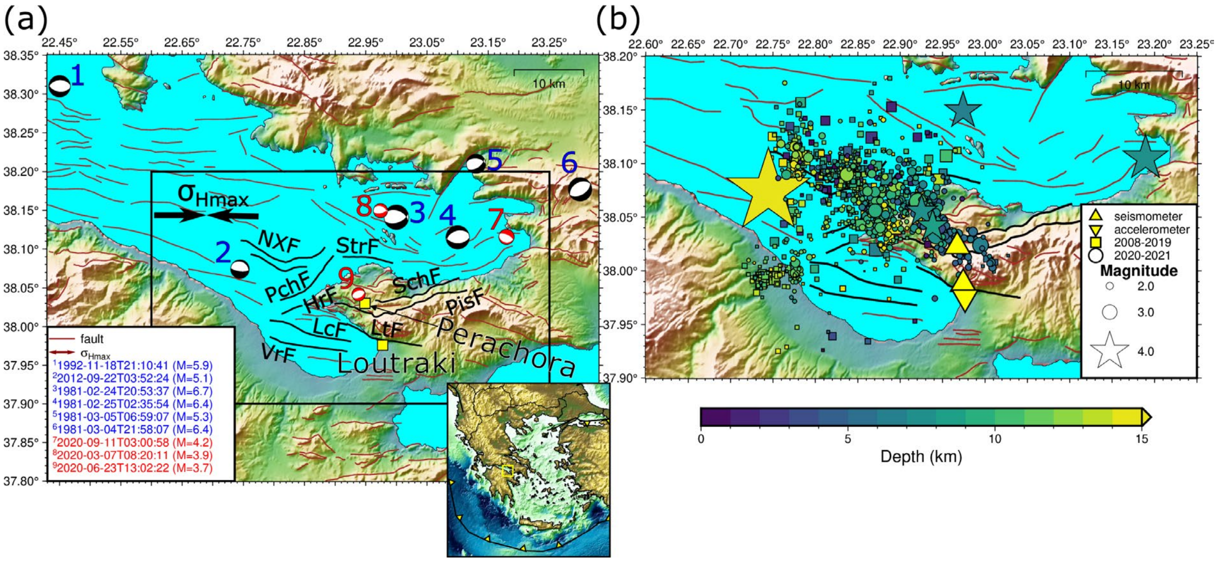

Figure 1. (a) Main tectonic features of the Eastern Gulf of Corinth. Beachballs show focal mechanisms for earthquakes of $M \geq 5.0$ that occurred after 1981 (blue) (after [Kapetanidis and Kassaras, 2019], apart from the 2012 event from [Mesimeri et al., 2018]) and the three strongest events of the 2020 crisis (red) [Michas et al., 2022]. The regional maximum horizontal compressive stress component (σ_{Hmax}) is also shown (black arrows) [Kapetanidis and Kassaras, 2019]. The black rectangle delineates the area in (b) and the yellow square shows the locations of Perachora and Loutraki towns. Faults (brown lines) after [Michas et al., 2015]. Faults important to the current study are named and marked by bold black lines; Heraion (HrF), Lechaio (LcF), Loutraki (LtF), North Xylocastro (NXF, two branches), Perachora (PchF), Pisia (PisF), Schinos (SchF), Strava (StrF) and Vrachati (VrF). Inset: the location of the region in (a) (yellow rectangle). (b) Earthquake locations of events in the vicinity of Loutraki that occurred before (squares) and during (circles) 2020-2021. Stars show $M > 4.0$ events (with the largest marking the 2012 $M_w = 5.1$ earthquake), while the sites of broadband seismometers (triangles) and an accelerometer (inverted triangle) are also exhibited. Faults as in (a).

~20 km NW of Loutraki at a depth of 16 km, being a rather rare case of a strong event [Mesimeri et al., 2018]. Starting in April 2020, an uncommon seismic crisis was recorded in the EGoC (Fig. 1b), extending approximately 20 km NW of Loutraki [Michas et al., 2022]. Initial activity was sparse and shallow (~ 6 km depth), located at the eastern part of the peninsula (east of HP.LTK). Seismicity started migrated west/northwest in May 2020, with an accelerated rate of ~3.3 events per day and increasing depths. On June 23rd, a $M_w = 3.7$ event occurred with a focal mechanism indicating a NW-dipping plane (Fig. 1a), perpendicular to the seismicity migration direction and the nearby faults (e.g. the western edge of Pisia). As seismicity propagated further west during July-August, the foci kept deepening. The inferred pore-fluid pressure diffusion front had a typical hydraulic diffusivity of 2.8 m^2/s and a slow constant velocity of 0.22 km/day over 50 days [Michas et al., 2022]. Seismicity during that period was bounded by Vrachati Fault (in the south) and likely occurred along a NW-dipping blind fault. A strong $M_L = 3.9$ event preceded the crisis on March 3rd and a $M_L = 4.2$ earthquake occurred on September 11th, revitalizing the activity in the area for a few weeks. However, neither of these two events was located in the immediate vicinity of the Perachora sequence (Figure 1). Even though the main migrating bulk of seismicity lasted between April and late August, activity was modest, but decaying, for the rest of the year and the first trimester of 2021. The 2020 outburst offers a unique opportunity to investigate shear-wave splitting in the area.

2. Data and Methods

To investigate the state of crustal anisotropy beneath Loutraki, we used an event catalog compiled from three sources: (a) the Seismological Laboratory of the National and Kapodistrian University of Athens (SL-NKUA), for the period between 2008 and 2019, (b) the Geodynamic Institute of the National Observatory of Athens (GI-NOA), for the same period, and (c) the relocated catalogue of Michas et al. [2022], for the 2020-2021 seismic crisis at the Perachora peninsula. The catalog included hypocentral locations, local magnitudes (M_L) and manually determined arrival times for 991 earthquakes with M_L between 0.6 and 4.9 (the M_w of the September 2012 event, being equal to 5.1, was estimated by Mesimeri et al. [2018]). Waveforms for these events were obtained from the European Integrated Data Archive (EIDA) node at GI-NOA (EIDA@NOA), which hosts data recorded by Greek infrastructure [Evangelidis et al., 2021], such as the Hellenic Unified Seismic Network (HUSN). The study period begins in 2008, as this year also marks the unification of the various Greek seismic networks into HUSN, improving the quality of earthquake hypocenter solutions and offering publicly available waveform data. We found metadata for four sensors in the area, according to EIDA@NOA. A velocimeter (LOUT) and accelerometer (LTRS) installed by SL-NKUA (HA network, https://doi.org/10.7914/SN/HA) and a joint velocimeter-accelerometer installation by the University of Patras (LTK, HP network, https://doi.org/10.7914/SN/HP), all belonging to the wider HUSN. Unfortunately, access to waveforms recorded by station HERA (velocimeter of the HL network, https://doi.org/10.7914/SN/HL) was restricted. Velocity waveform recordings were retrieved for 991 events. We applied a basic preprocessing scheme after retrieving the data, by removing the trend and mean of the signal. Data acquisition and preprocessing was executed with ObsPy [Beyreuther et al., 2010; Krischer et al., 2015]. We also performed a search for instances of missing arrival times in our catalogue, despite waveform data being available. To this purpose, we employed the deep-learning PhaseNet algorithm [Zhu and Beroza, 2019], using the pre-trained model provided by the authors. We only considered arrivals characterized by a 0.70 probability of being a shear-wave. This yielded automatic arrival-time picks for 78 out of the 991 events, in stations HP.LTK and HA.LOUT. To further increase the number of candidate arrivals, we used the EQCorrscan software [Chamberlain et al., 2018] to detect suitable signals using template-matching (for details see Appendix A). A total of 4,908 additional candidates were obtained, focusing on signals detected at station HP.LTK. It is noted that the hypocentral solutions and phase travel times of the templates were assigned to the corresponding detections, as it was often the case that the signal to noise ratio was not adequate to establish a single-event location solution for them.

The angle of incidence is a critical quantity for shear-wave splitting studies, as it is used in data selection. Considering the latter, the concept of the shear-wave window has been established since the 1980s [Evans, 1984; Booth and Crampin, 1985]. Shear-waves that arrive at the station with incident angles (i_h) larger than a critical value could be contaminated by the sP phase, i.e. a headwave occurring at the Earth's surface [Nuttli, 1961]. This critical angle can be calculated when the V_p/V_s ratio of the surficial layer is known [Evans, 1984]. In our case, the V_p/V_s ratio was determined as 1.76 [Michas et al., 2022] and, thus, the critical angle is equal to 35°. However, the existence of a surficial low velocity layer (e.g. sediments) could warp ray paths to steeper incidence angles and permit a broader window of 45° [Booth and Crampin, 1985; Crampin and Chastin, 2003; Cochran et al., 2006; Giannopoulos et al., 2015; Savage et al., 2016; Sharma et al., 2017; Zhang et al., 2018; Gao et al., 2019; Pastori et al., 2019; Kaviris et al., 2020; Kapetanidis et al., 2021]. We adopted the broader 45° window, as geological mapping indicates that station HP.LTK is located on top of alluvial sediments and, possibly, a layer of flysch, while HA.LOUT and HA.LTRS are installed on sediments [IGME, 1984].

To determine the angles of incidence, we used the velocity model of Michas et al. [2022], which was estimated using local earthquakes of the 2020 Perachora crisis. Surficial layers implied by IGME [1984] were omitted, as it was not possible to know their seismic velocities. We estimated the incidence angles of all direct shear-wave arrivals using the Pyrocko software [Heimann et al., 2017]. This led to 917 arrivals, in all stations, for events of the original catalogue, within the shear-wave window. In particular, the majority (597) belong to HP.LTK, while 328 suitable arrivals were found in HA.LOUT and 32 in HA.LTRS. For template-matching detections, 2,965 additional arrivals were found at HP.LTK, 102 at HA.LOUT and 2 at HA.LTRS. In total, 4,006 event-station pairs were eligible for analysis, according to the shear-wave window.

As a final preparatory step, we analyzed teleseismic P-wave recordings at HP.LTK and HA.LOUT to identify possible sensor misorientations, between 2008 and 2021, using the method of Braunmiller et al. [2020]. The algorithm aims to minimize P-wave energy in the transverse component, after rotating waveforms in trial backazimuths, for multiple earthquakes. A statistical analysis is then performed on the results to determine the azimuth of the horizontal component. For this test, we used events at epicentral distances ranging from 30° to 100° with a minimum magnitude of 6.0. Event information was retrieved from the FDSN service of the Incorporated Research Institutions for Seismology (IRIS). A bandpass filter of 0.1-1.0 Hz was applied to waveforms, before the analysis. This technique could not be used to identify the orientation at HA.LTRS, as the station is equipped with an accelerometer, suitable for strong motions. Out of 726 candidate events, 167 measurements were eligible in HP.LTK. At station HA.LOUT, 118 measurements were retrieved from 503 earthquakes. The analysis yielded no significant issues with the sensor's orientation at HP.LTK, with its value being N0°E ± 4°, confirming the results of Evangelidis et al. [2021]. On the other hand, the azimuth of the north-south component at HA.LOUT was found to be N350°E ± 5° (i.e. rotated 5° to 15° counterclockwise), in contradiction with the results of Evangelidis et al. [2021] who found a clockwise rotation of over 20°. This odd difference is discussed further later on, along with φ results at the station.

We analyzed recordings of the 4,006 eligible event-station pairs with the Pytheas software [Spingos et al., 2020] that offers a fully automated processing scheme. We selected the popular Eigenvalue method [Silver and Chan, 1991] combined with cluster analysis [Teanby et al., 2004]. In summary, the algorithm performs a shear-wave splitting measurement over a range of candidate signal windows, by rotating the horizontal traces to trial φ values between N0°E and N179°E, correcting for a candidate time-delay (in our parameterization, between 0 ms and 350 ms) and then estimating the covariance matrix of the two corrected waveforms. The splitting parameters pair that best minimizes the second eigenvalue of the covariance matrix is considered as the optimal. Then, after acquiring one pair for different signal windows, a cluster analysis algorithm searches for the optimal cluster and measurement, in the space defined by φ and t_d. The software also automatically grades each observation, by considering several factors: (a) the errors of φ and t_d and (b) the correlation coefficient of the unsplit waveforms. A score is calculated from these factors and a grade (with "A" being best and "E" being worst) is assigned. Moreover, if the polarization of the corrected shear-wave is sub-parallel or sub-perpendicular to φ, the measurement is considered null, as in those cases it cannot be decided whether the medium is isotropic or if the initial shear-wave polarization was the same as that of the fast or the slow shear wave polarization direction [Wüstefeld and Bokelmann, 2007]. Additionally, measurements with $t_d = 0$ ms are also considered null. These two tests are performed at the end of the grading algorithm, to measurements initially characterized "A", "B", "C" or "D". During the analysis, arrivals with a low Signal-to-Noise Ratio (SNR) are rejected. Filtering is also automated, with the range of the applied bandpass filter being determined by trying different frequency bandwidths and searching for the one that best removes noise, modified after the algorithm first introduced by Savage et al. [2010]. The complete parameterization used in our analysis is provided in Appendix B.

3. Results

After rejecting shear-wave arrivals due to low SNR and cases of failed splitting estimation, we obtained a catalogue of 3,646 shear-wave splitting measurements. Grading yielded 43 "A", 536 "B", 778 "C", 100 "D", 2,149 "E" and 40 null measurements. The high number of lower quality ("D" and "E") observations is due to the application of quality estimators (see Appendix B) and the low amplitudes of detections from template-matching. All 40 null measurements were observed at HP.LTK (see Appendix C). Hereafter, we only used "A", "B" and "C" quality parameters. Out of the three stations, HP.LTK presented the highest number of results with 1,311 accepted measurements. HA.LOUT offered 46 observations of quality "B" and "C", while the 2 measurements at HA.LTRS were both rejected (grade "E"). A summary of the average values for the two eligible stations are shown in Table 1. The normalized time-delays (t_n) were obtained after dividing each t_d with the corresponding hypocentral distance. To calculate their errors, we used the formula proposed by Del Pezzo et al. [2004] shown in Eq. (1):

$$\delta t_n = \sqrt{R^{-2}\delta t_d + R^{-4} t_d^2 \delta R \delta_R^2} \tag{1}$$

where R is the hypocentral distance, δt_d the time-delay estimation error and δR the error of the hypocentral distance. As opposed to Del Pezzo et al. [2004], we did not use fixed values for δt_d and δR, as we utilized the errors associated with each observation. It is noted that for the determination of splitting parameter errors Pytheas uses the revisited formulations of Walsh et al. [2013].

At HP.LTK, the polarization direction of the fast shear-wave shows a variety of measurements, with a clear dominant NW-SE orientation (Fig. 2a). However, we can also observe two significant concentrations of measurements striking ENE-WSW and N-S. The mean value (N105°E) is clearly affected, with the median of the sample being N111°E (closer to the main concentration seen in Figure 2a).

Parameter	HP.LTK	HA.LOUT
N	1,311	46
$\varphi \pm \sigma\varphi$ (°)	105 ± 43	164 ± 50
$t_d \pm \sigma_{td}$ (ms)	129 ± 70	157 ± 80
$t_n \pm \sigma_{tn}$ (ms/km)	15 ± 10	11 ± 6

Table 1. Average value and respective standard deviation (σ) for the polarization direction of the fast shear-wave (φ), the time-delay (t_d) and the normalized time-delay (t_n) at each station. The number of eligible observations (N) is also shown.

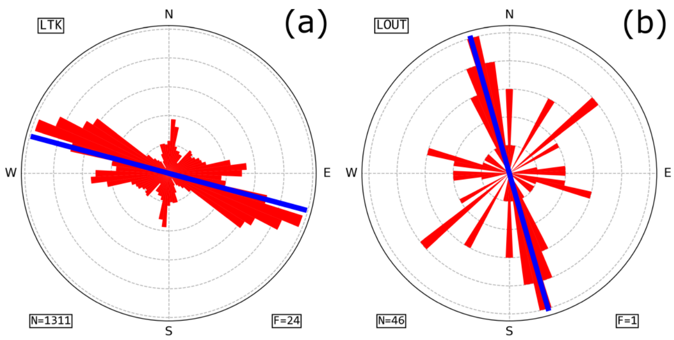

Figure 2. Rose diagram for results at HP.LTK (a) and HA.LOUT (b). Angles are binned every 5°. F indicates the interval of the grid. The blue line shows the mean direction of φ at each station.

On the other hand, HA.LOUT presents a dominant direction at NNW-SSE (Figure 2b). There are differing observations present, but they do not form a large concentration. In both cases, φ values in the rose diagrams are controlled by the results of the analyzed template-matching detections. In HP.LTK, 1,097 of the observations belong to detections (with 214 coming from original locations), while in HA.LOUT, only 3 out of the 46 measurements resulted from cases of initial hypocenters. Therefore, even though our broader dataset has considered events from 2008, there is strong bias towards the 2020-2021 era due to the dominance of the detections. Moreover, there is an ambiguity in the orientation of HA.LOUT. As explained earlier, the sensor could be misoriented either ~10° counterclockwise (according to our analysis) or ~20° clockwise (according to Evangelidis et al. [2021]). We have not corrected φ values for either case, due to the ambiguity and will consider this in interpreting the results. It is noted that the correction of Evangelidis et al. [2021] would result in a mean φ of ~N144°E, closer to the NW-SE direction of HP.LTK.

To identify and demonstrate spatial patterns of φ, we adopted a simple spatial averaging algorithm. First, TauP [Crotwell et al., 1999] was used to generate ray pierce points between the focus and the respective recording station, every 0.5 km of depth. Then, for each pierce point, the measured φ value was assigned, as well as the distance the ray travelled up to that point. For a grid with nodes spaced every 0.025° (for either latitude or longitude), the pierce points that belonged to the respective cell were retrieved. To acquire the mean φ we used the weighted averaging formula shown in Eq. (2), proposed by Johnson et al. [2011]:

$$\overline{\varphi_c} = \tan^{-1} 2 \left(\frac{\sum_{r=1}^{n} \sin(\varphi_r) * w_{rc}}{\sum_{r=1}^{n} w_{rc}}, \frac{\sum_{r=1}^{n} \cos(\varphi_r) * w_{rc}}{\sum_{r=1}^{n} w_{rc}} \right) \quad (2)$$

where r and c are the identifiers for each ray and grid cell, and w is the weighting function. We used $1/d^2$ to weight φ, with d being the distance between the station and the node. Grid cells with less than 5 pierce points were rejected. The standard deviation and error were also estimated. Nodes with a deviation over 30° and an error over 10° were considered ambiguous [Johnson et al., 2011]. We preferred to calculate averages for each station independently, because of the significant differences between the two. The number of observations at HP.LTK (1,311) is ~30 times greater than the one at HA.LOUT (46), which would eliminate any possible patterns existing at the latter. Moreover, there is the uncertainty about the orientation of HA.LOUT.

We observe significant differences between the western and southern edges of the grid and the nodes closer to the stations (Fig. 3). Averages in the south are mostly oriented either NE-SW (for HP.LTK) or NW-SE (for HA.LOUT). For HP.LTK, averages at the center and east of the area show a general ENE-WSW to E-W orientation, while at the northwestern edge a clear NE-SW direction is present. WNW-ESE to NW-SE observations (which coincide with the dominant φ seen in the rose diagram of Figure 2a) are mostly present to the northeastern edge, but can also be observed north of the station mixed with other directions. Averaging results for HA.LOUT are more limited due to the lack of measurements, but indicate NNW-SSE directions offshore that gradually shift to NW-SE closer to the station. The latter averages are very similar to observations at HP.LTK. In Figure 3, the two grid nodes to the south of HA.LOUT exhibit the same direction from measurements of either station (which causes the HA.LOUT vector to be drawn right above the HP.LTK one).

The distribution of time-delays (Figure 4) at HP.LTK shows a significant concentration between 100 and 130 ms, with similar decreases on either side. There are very few observations towards the limit imposed by the software parameterization (i.e. 350 ms). It is clear that t_d does not follow a normal distribution, when considering the average and standard deviation of Table 1. Similarly, normalized time-delays (Figure 4b) show an increase between

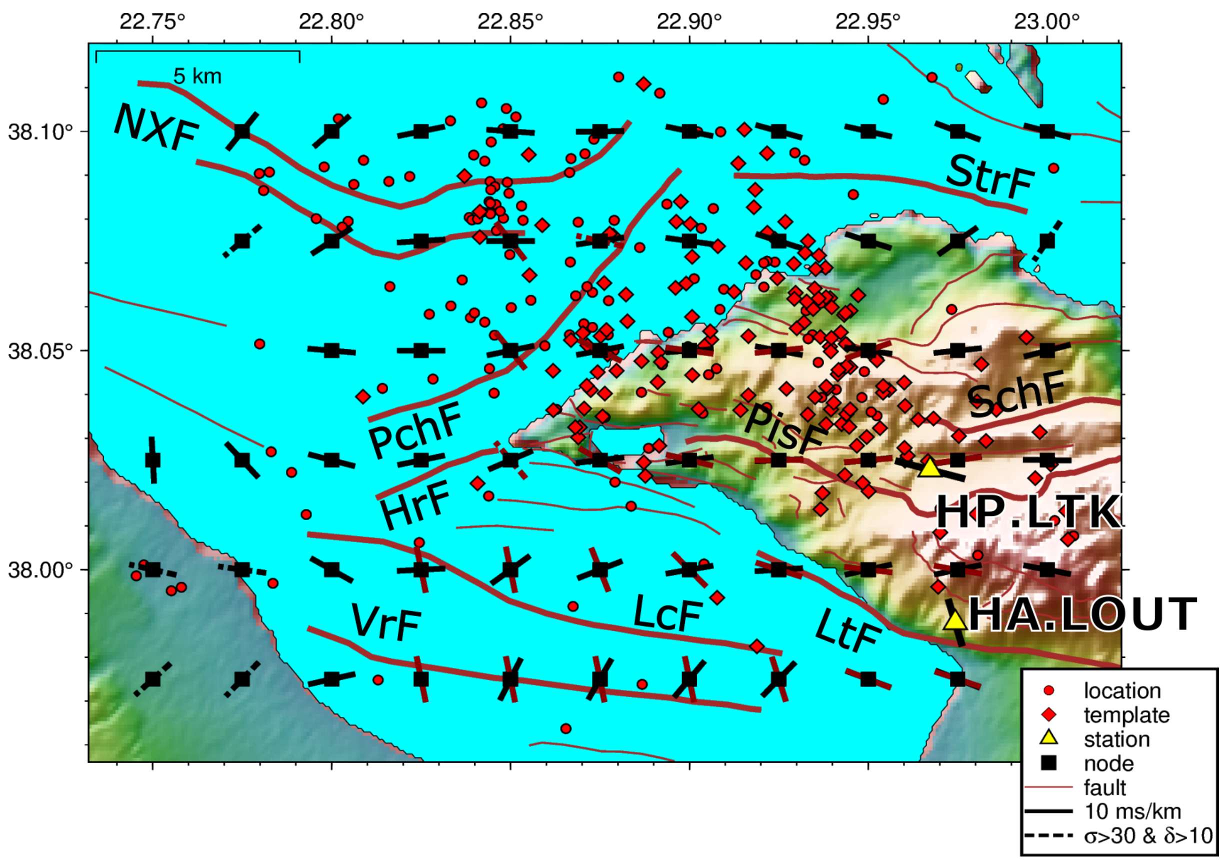

Figure 3. Spatial averaging for nodes (black squares) spaced every 0.025°, for results obtained at HP.LTK (black lines) and HA.LOUT (dark red lines). Dashed lines show averages with a standard deviation over 30° and an error larger than 10°. The vector length at each station (yellow triangles) is proportionate to the average t_n (see legend). Epicenters that provided at least one splitting measurement are marked by red circles (for original locations) or red diamonds (for templates). Faults (brown lines) after Michas et al. [2015].

14 and 18 ms/km and a steady decrease of observations towards the extreme end (> 30 ms/km). Understandably, t_n is greatly affected by the location of the epicenter and the focal depth. In the case of the EGoC, the sparsity of the network has an adverse effect on the quality of event solutions and, especially, the depth [Michas et al., 2022]. In addition, detections from template-matching could not be located and their source details depend on the quality of the template solution. These characteristics of the catalogue introduce significant qualitative uncertainties in t_n. The limited number of results at HA.LOUT does not permit a similar evaluation of the distribution of time-delays. Nevertheless, due to its furthest location from epicenters, HA.LOUT features high t_d observations (with ∼1/5 of them being over 250 ms), which then translate to modest t_n (only 1 measurement exceeds 20 ms/km).

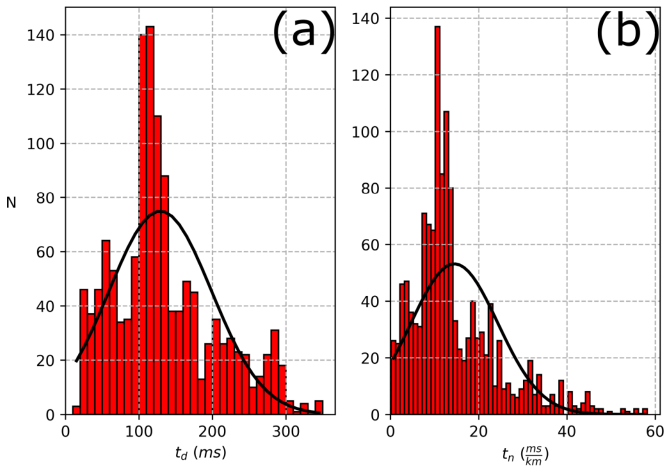

Figure 4. Distribution of time-delays (a) and normalized time-delays (b) for station HP.LTK. The black line shows the fitted normal distribution for these parameters. t_d is binned by 10 ms (1 sample) and t_n by 1 ms/km. N is the count of observations per bin.

4. Discussion

4.1 Spatial patterns of φ in the EGoC

The study area of the eastern edge of the Gulf of Corinth is characterized by extension in a, grossly, NNE-SSW direction [Jackson et al., 1982; Roberts and Koukouvelas, 1996; Sachpazi et al., 2003]. Stress inversion from regional focal mechanisms has shown that the maximum horizontal compressive stress component (σ_{Hmax}) is oriented parallel to the greater rift structure, i.e. approximately WNW-ESE [Kapetanidis and Kassaras, 2019; Kassaras et al., 2020]. Theoretically, if the crust around Loutraki and Perachora is permeated by fluid-filled microcracks, it is expected that they align to this direction, in response to the applied stress field [Crampin et al., 1984; Crampin, 1987; Crampin and Chastin, 2003; Crampin and Peacock, 2005], which, in turn, would be reflected in the rose diagram of Fig. 2. In HP.LTK, we see that this is the direction that prevails, even though there is a strong presence of ENE-WSW and NNE-SSW observations. On the contrary, the main direction at HA.LOUT deviates significantly from the orientation of σ_{Hmax}. If we consider the ∼20° clockwise sensor drift of Evangelidis et al. [2021], the φ values better fit with the regional stress field (as the average φ would be N144°E). The well-constrained N350°E ± 5° seismometer orientation that we found would rotate the results the other way, closer to N-S (N174°E). While the former correction suits splitting interpretation better, we cannot confidently reject the latter case and, therefore, did not apply any correction to our data observations. This is an open question that could be definitively answered in the future, by field measurements of the true north.

Local studies in other areas of the EGoC have shown a prevalence of NW-SE polarizations, mostly agreeable with σ_{Hmax}, with one exception of a second φ direction, oriented NE-SW [Papadimitriou et al., 1999; Kaviris, 2003; Kaviris et al., 2014]. In the Western Gulf of Corinth, there have been observations of odd NE-SW polarization directions, but most polarizations are compatible with σ_{Hmax} [e.g. Giannopoulos et al., 2015; Kaviris et al., 2017].

Similar cases of disassociation of φ with the local stress field have been reported to other areas, where the role of local faults in controlling the polarization direction has been recognized [Cochran et al., 2003, 2006; Liu et al., 2008; Gao et al., 2011, 2019; Sharma et al., 2017; Kaviris et al., 2021]. Therefore, disagreements between φ and the regional stress are reported even in some cases where more than one dominant polarization direction are observed at the same station. In our case, there seems to be a spatial (but not azimuthal) variation, with average φ strongly deviating at the edge of the area, while otherwise being constrained in a WNW-ESE to ENE-WSW range. There is some correlation with existing structures, as in the cases of the Heraion and Strava faults. However, there is no clear alignment with faults in the rest of the area and there are cases where φ is perpendicular to the nearby fault, as in the south (Lechaio and Vrachati faults) and the western edge of the North Xylocastro fault. Considering station averages, the NW-SE direction at HA.LOUT agrees with the nearby Loutraki fault (even more so if the correction of Evangelidis et al. [2021] is applied). HP.LTK on the other hand is surrounded by diverse faults such as the ~E-W-striking Schinos and the complex Pisia faults. The absence of a strong connection between the spatial distribution of φ and local faults leads us to believe that stress or pressure gradients, as modelled by APE, are the main controlling factors of anisotropy in the area. The main direction of S_{fast} polarization in HP.LTK and (potentially) HA.LOUT is almost parallel to σ_{Hmax}.

4.2 Temporal variations before the crisis

We then attempted to identify temporal patterns of splitting parameters, associated with the occurrence of significant earthquakes. Time-delays have long been hypothesized to function as a proxy of stress concentration and release, in a rock volume [Peacock et al., 1988; Crampin, 1998; Gao and Crampin, 2003; Crampin et al., 2008]. Accumulation of tectonic stress affects the crustal microcracks by shifting their aspect-ratio and opening new ones. As stress increases, it may reach a critical threshold where cracks coalesce, leading to the eventual earthquake. This behavior has been modelled by the Anisotropic Poro-Elasticity (APE) and was also supported by empirical data [Crampin and Zatsepin, 1997; Zatsepin and Crampin, 1997], suggesting a physical background to possible "stress-forecast" strong events [Crampin, 2011; Crampin et al., 2013]. Therefore, we would expect an abrupt change in the polarization direction of the S_{fast} (due to the shift in aspect-ratio) before an earthquake (a so-called 90°-flip), while the event would be preceded by a long period of time-delay increase and a short time of decrease, respective to stress accumulation and release (due to coalescence). Volcanic regimes, where magma and other hot fluids circulate causing violent eruptions, have been a natural laboratory for shear-wave splitting, as temporal and spatial variations of φ (including 90°-flips) and t_d have been well-recorded to function as precursors [Bianco et al., 2006; Bianco and Zaccarelli, 2009; Liu et al., 2014]. On the other hand, shear-wave splitting as a mean of earthquake prediction has come under scrutiny. Crampin et al. [1999] documented a successful stress-forecast of a M = 5.0 shock, with a 2-week lead time. However, their claim has been debated by Seher and Main [2004], who offered a statistical evaluation of the alleged forecast and reported significant uncertainties, even though they did not reach a firm conclusion, citing the high scatter of observations, possibly due to different ray paths. Other authors have identified variations of time-delays that were apparently random and did not coincide with the occurrence of an earthquake [Peng and Ben-Zion, 2004; Kaviris et al., 2017]. Regardless, the feat of Crampin et al. [1999] has not been repeated, as only posterior reports of inferred accumulation and relaxation sequences before a strong earthquake have been mentioned in literature [Gao and Crampin, 2004, 2006; Polat et al., 2012; Crampin et al., 2015; Kaviris et al., 2018b, 2018c, 2021]. In tectonic regimes, 90°-flips were reported by Padhy and Crampin [2006], interpreted as the existence of high pore pressure in the sampled rock volume, and have also been connected to wastewater injections [Nolte et al., 2017].

Concerning the temporal variations of splitting parameters, we attempted to identify abrupt changes that might be associated with significant events. We did not distinguish between Band-1 and Band-2 ray paths [Crampin et al., 1999], as the scatter in φ poses a great challenge in determining the true orientation of the crack plane and, in the case of pre-2020 measurements, the number of observations is already low. Following, temporal variations are examined in two periods: (a) between 2008 and 2019 and (b) during the 2020-2021 crisis. We focus on station HP.LTK, as HA.LOUT features only 3 measurements pre-2020. Finally, temporal variations were examined on daily-averaged data, to partially account for the expected high scatter in time-delays [Crampin et al., 2004]. For 2008-2019, the 80 observations at HP.LTK correspond to 71 days.

In terms of φ, observations for the overall period between 2008 and 2019 (Figure 5b) indicate a NE-SW trend with significant scattering through the years. In fact, the main direction of φ seems to be oriented NE-SW, almost perpendicular to the NW-SE direction acquired from the whole dataset (Figure 2a). There is a significant rotation in φ from ~N105°E (starting 2008) to ~N60°E (from approximately November 2014). According to the sensor orientation analysis detailed earlier, we did not find any changes in the seismometer's azimuth. Additionally, available metadata for HP.LTK do not document a change of sensors during 2014. Therefore, we can exclude misorientation as the cause of this change. Spatial dependence can also be excluded, as the epicenters of the 2008-2019 splitting observations are located in the area roughly formed by the significant earthquakes (black stars) in Figure 5c (also see Figure 1b). Temporally, the rotation of φ preceded the occurrence of a $M_L = 3.2$ event on the 22nd of February 2015, located ~12 km NW of HP.LTK at a depth of 11 km (small red star in Fig. 5c). According to APE, changes in pressure gradients resulting from fluid-related processes have an explicit effect on microcracks and, consequently, shear-wave splitting. As the $M_L = 3.2$ event occurred in the immediate vicinity of the station, we hypothesize that an increase in pore pressure could cause the φ changes seen. Seemingly, there is an increase of normalized time-delays in the period right before the sudden change in φ, which is followed by a decrease. According to its location, the $M_L = 3.2$ earthquake is likely the result of a rupture on a NE-SW oriented fault patch (whether on the eastern edge of a North Xylocastro fault branch or on the Perachora fault, as shown in Fig. 5c). The beginning of the alleged increase of t_n is on December 2013 and the start of the NE-SW-oriented φ is on October-November 2014. Fluid migration along a NE-SW pressure gradient could explain the shift in φ, the increase in t_n and the occurrence of the $M_L = 3.2$ event, possibly followed by gradual stress relaxation. Kim and Kim [2022] reported fast polarizations aligned to fluid flow, near gas production wells (i.e. a better monitored environment), evidencing the behavior modelled by APE. Unfortunately, the lack of a dense local network and, hence, the small number of detected earthquakes cannot establish whether these observations belong to a long-lasting pore-pressure diffusion episode, as the 15-month-long one observed in the western part of the Gulf during 2013-2014 [Kapetanidis et al., 2021]. There does not seem to be any significant change in splitting related to the February 2012 $M_L = 4.2$ earthquake located ~24 km SW of HP.LTK or the September 2012 $M_w = 5.1$ event (25 km NW of the station). The period between 2008 and 2010 features a plethora of $M_L > 3.0$ earthquakes NW of the station (black stars in Fig. 5c), but the lack of observations does not permit us to identify any related patterns.

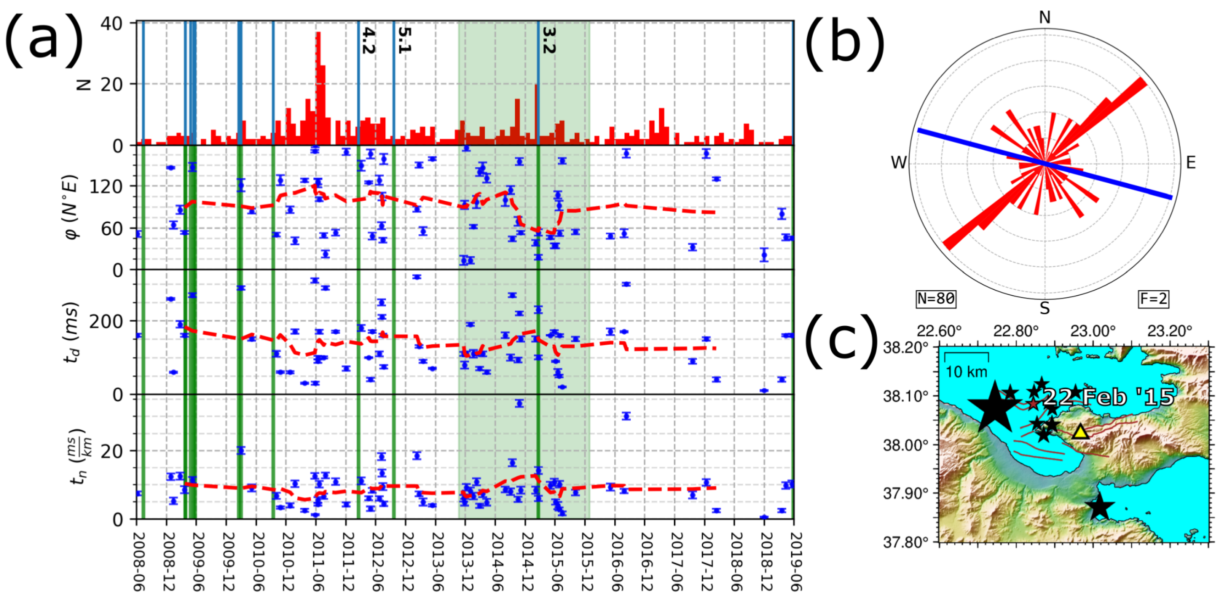

Figure 5. (a) Temporal variations of (from top to bottom) monthly seismicity, φ, t_d and t_n between 2008 and 2019 (daily average splitting parameters for HP.LTK). Each observation is accompanied by its respective error. The red dashed line indicates a 9-point moving average. Vertical solid lines denote the occurrence of significant earthquakes ($M_L > 3.0$). The period of changes in SwS is shaded. (b) Rose diagram for measurements at HP.LTK between 2008 and 2019 (notation as in Fig. 2). (c) Map showing the significant earthquakes of (a) as black stars. The 2012 $M_L = 4.2$ and the 2015 $M_L = 3.2$ earthquakes are shown as red stars. Brown lines show the named faults of Figure 3.

4.3 Temporal variations during the crisis

The 1,231 observations in HP.LTK during 2020-2021 correspond to 125 daily averages. The seismicity outburst started in mid to late April 2020 (accompanied by the occurrence of a $M_L = 3.2$ event, Figure 6a). The number of earthquakes was reduced significantly after September 2020. Michas et al. [2022] identified earthquake migration along a N103°E axis between April and August. Vertically, seismicity deepened as migration progressed. Michas et al. [2022] suggest that it was triggered by fluid overpressures and evolved due to pore pressure gradients along local faults. Temporal variations of φ show a radical shift from N-S to NE-SW directions between March and April 2020 to approximately WNW-ESE in May. Then, there is great scatter in the dataset, with a strong presence of both WNW-ESE and NE-SW observations (Figure 6a). Time-delays show an increasing trend, starting on April. Variations of t_n directly contrast this, with an increase between March and the start of May followed by a month-long decrease and, then, a small increase in June followed by a clear decrease between the end of the month and September (possibly October). The apparent contradiction between t_d and t_n can be explained by the increasing hypocentral distances, as seismicity migrated away from HP.LTK and in greater depths. As t_d is assumed to be accumulated along the path, it is expected for its values to be highest when sources are the furthest from the station.

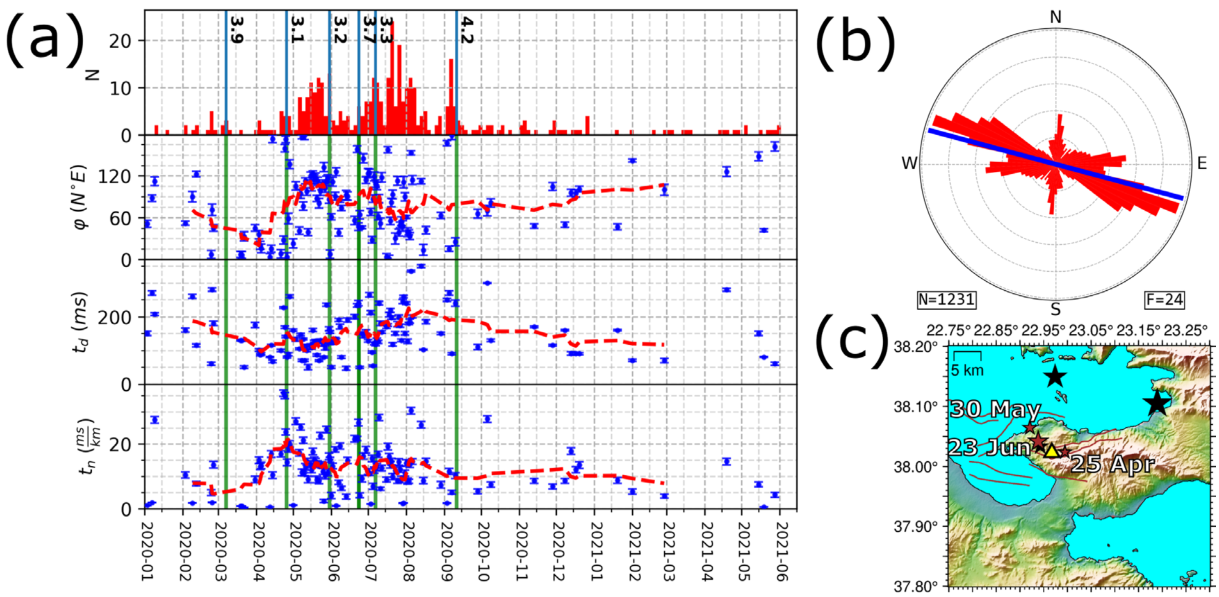

Figure 6. (a) Temporal variations of (from top to bottom) seismicity (bins every 3 days), φ, t_d and t_n between January 2020 and June 2021 (daily average splitting parameters for HP.LTK). (b) Rose diagram for measurements at HP.LTK for the same period. (c) Map showing the significant earthquakes of (a) as black stars. The April $M_L = 3.2$, May $M_L = 3.2$ and June $M_L = 3.7$ earthquakes are shown as red stars. Notation as in Fig. 5.

The shift in S_{fast} directions coincided with the first t_n increase, the occurrence of the late April $M_L = 3.1$ event ~2 km east of HP.LTK (Fig. 6c) and the beginning of the crisis. Nevertheless, the t_n increase started earlier, within March, and reached its peak (~36 ms/km) four days before the earthquake. Polarization direction abruptly shifted approximately 5 days later, while t_n were decreasing and seismicity was migrating west of HP.LTK. A group of φ values roughly ranging between N90°E and N120°E and the t_n decrease lasted until the occurrence of a $M_L = 3.2$ event ~6 km NW of the station on May 30th. From then on, there is high scatter in φ valuesand t_n increases until the June 23rd $M_L = 3.7$ event, located ~3 km NW of HP.LTK. Onwards, the φ scatter becomes more pronounced, while there's a well-defined t_n decrease. A new burst of seismicity (accompanied by a $M_L = 4.2$ earthquake ~21 km NE) in September does not seem to have any effect on splitting.

The changes preceding the April 25th $M_L = 3.1$ event (and the start of the crisis) do not seem to agree with literature. Normalized time-delays for small earthquakes ($M < 4.0$) have been reported before, but the stress accumulation and relaxation periods are much shorter, in the order of hours or days, as seen in the summary provided by Crampin et al.

[2013]. In our case, the increase lasts for a month and the decrease takes place in five days. Additionally, significant φ changes have not been reported as precursory phenomena for tectonic earthquakes, except for Padhy and Crampin [2006]. However, we observe a significant change in our case. The ~NE-SW polarization directions observed in December 2014 (Figure 5a) are similar to the ones seen between March and May 2020. The first trimester of 2020 (January-March) presents highly scattered φ. Unfortunately, there are either too few scattered observations (after 2015), or none at all (in the last semester of 2019), which makes connecting the two periods hardly possible. Data of the 2020-2021 group lead us to reconsider the hypothesis of a NE-SW migrating fluid front in 2014-2015. We propose two possible scenarios.

In the first, shear-wave splitting during 2014-2015 was indeed related to a lesser fluid migration episode along a NE-SW pressure gradient, which led to either low seismicity or mostly weak earthquakes that occurred well within the gulf, beyond the detectability of the regional network (which explains the lack of events in the catalogue). The period before April 2020 is also witnessing such an episode, which is then followed by the major (and more violent) crisis, with fluids migrating WNW-ESE.

According to the second scenario, anisotropy in the area is generally controlled by the offshore NE-SW-trending faults (e.g. the major Perachora fault). In this case, minor pressure gradients are the cause of scatter in φ before the crisis, while after April 2020 the major diffusion episode is the controlling factor of shear-wave splitting.

The complexity of interpreting anisotropy in the EGoC arises from the similarity of directions between different candidate factors. The prevalent WNW-ESE to NW-SE φ are comparable to σ_{Hmax}, fault strikes in the immediate vicinity of HP.LTK (e.g. Pisia) and the implied high pressure gradient associated with the 2020 seismicity, all of which have the same direction. If the S_{fast} polarization was the result of the effect of local faults, it would not change significantly over time, considering the similarity in the backazimuths of the various events. Moreover, the fault systems closer to the station should have imposed their orientation on φ, as in other cases where structurally-controlled anisotropy is observed [e.g. Li and Peng, 2017; Gao et al., 2019; Pastori et al., 2019; Shi et al., 2020; Ortega-Romo, 2021]. Finally, we found no convincing evidence of spatial correlation between faults and spatially averaged polarizations (Figure 3). Changes in φ controlled by σ_{Hmax} could be associated with 90°-flips, when the medium reaches fracture criticality, as modelled by APE. However, a strong presence of the direction perpendicular to the dominant WNW-ESE (~N20°E) is noticeably absent (Figures 2, 5b and 6b), while highly scattered φ values are commonly present. High pressure gradients have been shown to cause unconformable observations of φ [e.g. Kim and Kim, 2022]. Therefore, we favor the first scenario of diffusion episodes of different intensity and directivity as the driving force behind anisotropy in the EGoC. During 2020, increases and decreases of t_n mark three sub-episodes of fluid migration, highlighted by the occurrence of $M > 3.0$ earthquakes. However, there seem to be narrow spatial constraints, as only events in epicentral distances of less than 12 km had a detectable footprint on shear-wave splitting. The two strong $M_L = 4.2$ earthquakes (in 2012 and 2020) and the much stronger $M_w = 5.1$ event of 2012, that occurred over 20 km away, had no effect on observations.

5. Conclusions

Analysis of 13 years of earthquakes in the Eastern Gulf of Corinth, recorded by broadband stations HP.LTK and HA.LOUT, located near Loutraki, led to the identification of a complex shear-wave splitting regime. After considering the limit of the shear-wave window and other criteria, eligible observations revealed a dominant NW-SE direction with a strong secondary NE-SW and a N-S orientation also present. Spatial averaging did not reveal any clear links between local structures and these directions. However, significant temporal patterns of both φ and t_n were discovered, related to four events, in HP.LTK; (a) a $M_L = 3.2$ earthquake on February 2015, (b) a $M_L = 3.1$ earthquake on April 2020, (c) a $M_L = 3.2$ event on May 2020 and (d) a $M_L = 3.7$ earthquake on June 2020. All these events were located at a maximum epicentral distance of 12 km, while the strongest events in the catalogue (on February 2012 and September 2020, both $M_L = 4.2$, and on September 2012 with $M_w = 5.1$) had no effect on splitting. We suggest that anisotropy in the area is controlled by pressure gradients related to episodic fluid diffusion, as the 2020 variations follow seismicity changes and a well-defined NW-SE seismicity migration front. However, the existence of a long NE-SW pressure gradient during 2014-2015 can only be theorized, as there is no evidence from seismicity. The spatial independence of φ and the temporal changes in splitting parameters ruled out structurally-controlled anisotropy, while the existence of a prevalent NE-SW direction before the 2020 shows that the dominant φ being parallel to σ_{Hmax}, during the crisis, could be coincidental. SwS in the EGoC seems to be more complex than in the Western Gulf of Corinth. In the latter, φ directions generally agree with either σ_{Hmax} or local faulting [e.g. Giannopoulos et al., 2015; Kaviris et al., 2017, 2018; Kapetanidis et al., 2021].

Template-matching was critical in increasing available arrivals at HP.LTK, during the 2020 outburst. A detailed seismotectonic study (possibly integrating template-matching) for 2014 and 2015 could reveal additional earthquakes and permit the analysis of seismicity to determine whether fluids played a role in the upper crust anisotropy during that period.

Acknowledgments. The authors are deeply grateful to the two reviewers for their invaluable advice and the suggestion to use template-matching to increase the availability of data. We would also like to thank the staff supporting the Hellenic Unified Seismic Network, and particularly the Seismological Laboratory of the University of Patras for installing and operating station HP.LTK (https://doi.org/10.7914/SN/HP). We also thank the personnel of SL-NKUA and GI-NOA that participates in the daily manual determination of arrival times, and for freely offering their earthquake catalogs.

Funding. This study was partially supported by the Hellenic Foundation for Research and Innovation (H.F.R.I.) under the "2nd Call for H.F.R.I. Research Projects to support Post-Doctoral Researchers" (Project Number: 00256).

Data and sharing resources. Waveform recordings, station metadata, as well as the earthquake catalog of GI-NOA, were acquired from the EIDA node at GI-NOA (http://eida.gein.noa.gr/). The event catalog of NKUA-SL is available at http://www.geophysics.geol.uoa.gr/stations/gmapv3_db/index.php?lang = en.
Angles of incidence and travel times were computed with Pyrocko's Cake (https://pyrocko.org/). The sensor orientation of HP.LTK was estimated using the OrientPy package (https://github.com/nfsi-canada/OrientPy). Automatic picks were acquired with PhaseNet (https://github.com/wayneweiqiang/PhaseNet). The shear-wave splitting analysis was carried out by the Pytheas software (https://github.com/ispingos/pytheas-splitting). Circular statistics were computed with pycircstat (https://github.com/circstat/pycircstat). EQcorrscan was used to detect arrivals through template-matching (https://github.com/eqcorrscan/EQcorrscan).
Figures 1 and 3 were plotted with the Generic Mapping Tools, v.6.3.0 package [Wessel et al., 2019] and its Python wrapper, PyGMT [Uieda et al., 2021]. Other figures were plotted with Matplotlib [Hunter, 2007]. All figures were edited with Inkscape (https://inkscape.org/).

References

Abt, D.L. and K.M. Fischer (2008) Resolving three-dimensional anisotropic structure with shear wave splitting tomography, Geophys. J. Int., 173, 859-886, https://doi.org/10.1111/j.1365-246X.2008.03757.x

Adelinet, M., C. Dorbath, M. Calò, L. Dorbath and M. Le Ravalec (2016). Crack Features and Shear-Wave Splitting Associated with Fracture Extension during Hydraulic Stimulation of the Geothermal Reservoir in Soultz-sous-Forêts, Oil Gas Sci. Technol. Rev. d'IFP Energies Nouv., 71, 39, https://doi.org/10.2516/ogst/2015023

Ambraseys, N. (2015). Earthquakes in the mediterranean and middle east: A multidisciplinary study of seismicity up to 1900, Cambridge University Press. https://doi.org/10.1017/CBO9781139195430

Audoine, E., M. K. Savage and K. Gledhill (2004). Anisotropic structure under a back arc spreading region, the Taupo Volcanic Zone, New Zealand, J. Geophys. Res. Solid Earth, 109, 1-21. https://doi.org/10.1029/2003JB002932

Berens, P. (2009). CircStat: a MATLAB toolbox for circular statistics, J. Stat. Softw., 31.

Bernard, P., G. Chouliaras, A. Tzanis, P. Briole, M. P. Bouin, J. Tellez, G. Stavrakakis and K. Makropoulos (1997). Seismic and electrical anisotropy in the Mornos delta, Gulf of Corinth, Greece, and its relationship with GPS strain measurements, Geophys. Res. Lett., https://doi.org/10.1029/97GL02102

Beyreuther, M., R. Barsch, L. Krischer, T. Megies., Y. Behr and J. Wassermann (2010). ObsPy: A Python Toolbox for Seismology, Seismol. Res. Lett., 81, 530 LP – 533.

Bianco, F., L. Scarfı, E. Del Pezzo, D. Patanè (2006). Shear wave splitting changes associated with the 2001 volcanic eruption on Mt Etna, Geophys. J. Int., 167, 959-967, https://doi.org/10.1111/j.1365-246X.2006.03152.x

Bianco, F. and L. Zaccarelli (2009). A reappraisal of shear wave splitting parameters from Italian active volcanic areas through a semiautomatic algorithm, J. Seismol., 13, 253-266, https://doi.org/10.1007/s10950-008-9125-z

Booth, D. and S. Crampin (1985). Shear-wave polarizations on a curved wavefront at an isotropic free surface, Geophys. J. Int., 31-45.

Bouin, M.-P., J. Téllez, P. Bernard (1996). Seismic anisotropy around the Gulf of Corinth, Greece, deduced from three-component seismograms of local earthquakes and its relationship with crustal strain, J. Geophys. Res. Solid Earth, 101, 5797-5811, https://doi.org/10.1029/95JB03464

Braunmiller, J., J. Nabelek and A. Ghods (2020). Sensor orientation of Iranian broadband seismic stations from P-wave particle motion, Seismol. Res. Lett., 91, 1660-1671. https://doi.org/10.1785/0220200019

Chamberlain, C.J., C.J. Hopp, C.M. Boese, E. Warren-Smith, D. Chambers, S.X. Chu, K. Michailos and J. Townend (2018). EQcorrscan: Repeating and Near-Repeating Earthquake Detection and Analysis in Python, Seismol. Res. Lett., 89, 173-181. https://doi.org/10.1785/0220170151

Chen, X., V. Levin and H. Yuan (2021). Small Shear Wave Splitting Delays Suggest Weak Anisotropy in Cratonic Mantle Lithosphere, Geophys. Res. Lett., 48, e2021GL093861, https://doi.org/10.1029/2021GL093861

Cochran, E.S., Y. G. Li and J.E. Vidale (2006). Anisotropy in the shallow crust observed around the San Andreas fault before and after the 2004 M 6.0 Parkfield earthquake, Bull. Seismol. Soc. Am., 96, 364-375, https://doi.org/10.1785/0120050804

Cochran, E.S., J.E. Vidale and Y.G. Li (2003). Near-fault anisotropy following the Hector Mine earthquake, J. Geophys. Res. Solid Earth, 108, https://doi.org/10.1029/2002jb002352

Crampin, S. (2011). Shear-Wave Splitting: New Geophysics and Earthquake Stress-Forecasting, in: Gupta, H.K. (Ed.), Encyclopedia of Solid Earth Geophysics, Springer, Dordrecht, https://doi.org/10.1007/978-90-481-8702-7

Crampin, S. (1987). Geological and industrial implications of extensive-dilatancy anisotropy. Nature 328, 491-496. https://doi.org/10.1038/328491a0

Crampin, S. (1998). Stress-forecasting: a viable alternative to earthquake prediction in a dynamic Earth, Earth Environ. Sci. Trans. R. Soc. Edinburgh, 89, 121-133. https://doi.org/10.1017/S0263593300007057

Crampin, S. and B. K. Atkinson (1985). Microcracks in the Earth's crust, First Break 3. https://doi.org/10.3997/1365-2397.1985005

Crampin, S. and S. Chastin (2003). A review of shear wave splitting in the crack-critical crust, Geophys. J. Int. 155, 221-240. https://doi.org/10.1046/j.1365-246X.2003.02037.x

Crampin, S., R. Evans, B. K. Atkinson (1984). Earthquake prediction: a new physical basis. Geophys. J. Roy. Astr. S. 76, 147-156. https://doi.org/10.1111/j.1365-246X.1984.tb05030.x

Crampin, S., Y. Gao, J. Bukits (2015). A review of retrospective stress-forecasts of earthquakes and eruptions, Phys. Earth Planet. Inter. 245, 76-87, https://doi.org/10.1016/j.pepi.2015.05.008

Crampin, S., Y. Gao and A. De Santis (2013) A few earthquake conundrums resolved, J. Asian Earth Sci., 62, 501-509, https://doi.org/10.1016/j.jseaes.2012.10.036

Crampin, S., Y. Gao and S. Peacock (2008). Stress-forecasting (not predicting) earthquakes: A paradigm shift, Geology, 36, 427, https://doi.org/10.1130/G24643A.1

Crampin, S. and S. Peacock (2005). A review of shear-wave splitting in the compliant crack-critical anisotropic Earth, Wave Motion, 41, 59-77, https://doi.org/10.1016/j.wavemoti.2004.05.006

Crampin, S., S. Peacock, Y. Gao, and S. Chastin (2004). The scatter of time-delays in shear-wave splitting above small earthquakes, Geophys. J. Int., 156, 39-44, https://doi.org/10.1111/j.1365-246X.2004.02040.x

Crampin, S., T. Volti and R. Stefánsson (1999). A successfully stress-forecast earthquake, Geophys. J. Int., 1-5.

Crampin, S. and S. Zatsepin (1997). Modelling the compliance of crustal rock—II. Response to temporal changes before earthquakes, Geophys. J. Int. 129, 495-506. https://doi.org/10.1111/j.1365-246X.1997.tb04489.x

Crotwell, H. P., T.J. Owens and J. Ritsema (1999). The TauP Toolkit: Flexible Seismic Travel-time and Ray-path Utilities, Seismol. Res. Lett., 70, 154-160, https://doi.org/10.1785/gssrl.70.2.154

Del Pezzo, E., F. Bianco, S. Petrosino and G. Saccorotti (2004). Changes in the coda decay rate and shear-wave splitting parameters associated with seismic swarms at Mt. Vesuvius, Italy, Bull. Seismol. Soc. Am., 94, 439-452. https://doi.org/10.1785/0120030141

Evangelidis, C.P. (2017). Seismic anisotropy in the Hellenic subduction zone: Effects of slab segmentation and subslab mantle flow, Earth Planet. Sci. Lett., 480, 97-106, https://doi.org/10.1016/j.epsl.2017.10.003

Evangelidis, C.P., N. Triantafyllis, M. Samios, K. Boukouras, K. Kontakos, O. J. Ktenidou, I. Fountoulakis, I. Kalogeras, N. S. Melis, O. Galanis, C. B. Papazachos, P. Hatzidimitriou, E. Scordilis, E. Sokos, P. Paraskevopoulos, A. Serpetsidaki, G. Kaviris, V. Kapetanidis, P. Papadimitriou, N. Voulgaris, I. Kassaras, G. Chatzopoulos, I. Makris, F. Vallianatos, K. Kostantinidou, C. Papaioannou, N. Theodoulidis, B. Margaris, S. Pilidou, I. Dimitriadis, P. Iosif,

M. Manakou, Z. Roumelioti, K. Pitilakis, E. Riga, G. Drakatos, A. Kiratzi, G. A.Tselentis (2021). Seismic Waveform Data from Greece and Cyprus: Integration, Archival, and Open Access, Seismol. Res. Lett., 92, 1672-1684, https://doi.org/10.1785/0220200408

Evans, R. (1984). Effects of the free surface on shear wavetrains, Geophys. J. Int., 76, 165-172, https://doi.org/10.1111/j.1365-246X.1984.tb05032.x

Gao, Y., A. Chen, Y. Shi, Z. Zhang, L. Liu (2019). Preliminary analysis of crustal shear-wave splitting in the Sanjiang lateral collision zone of the southeast margin of the Tibetan Plateau and its tectonic implications, Geophys. Prospect., 67, 2432-2449, https://doi.org/10.1111/1365-2478.12870

Gao, Y. and S. Crampin (2006). A stress-forecast earthquake (with hindsight), where migration of source earthquakes causes anomalies in shear-wave polarisations, Tectonophysics, 426, 253-262, https://doi.org/10.1016/j.tecto.2006.07.013

Gao, Y. and S. Crampin (2004). Observations of stress relaxation before earthquakes, Geophys. J. Int., 157, 578-582, https://doi.org/10.1111/j.1365-246X.2004.02207.x

Gao, Y. and S. Crampin (2003). Temporal variations of shear-wave splitting in field and laboratory studies in China, J. Appl. Geophys., 54, 279-287, https://doi.org/10.1016/j.jappgeo.2003.01.002

Gao, Y., J. Wu, Y. Fukao, Y. Shi and A. Zhu (2011). Shear wave splitting in the crust in North China: stress, faults and tectonic implications, Geophys. J. Int. 187, 642-654, https://doi.org/10.1111/j.1365-246X.2011.05200.x

Giannopoulos, D., E. Sokos, K.I. Konstantinou and G. A. Tselentis (2015). Shear wave splitting and V_P/V_S variations before and after the Efpalio earthquake sequence, western Gulf of Corinth, Greece, Geophys. J. Int., 200, 1436-1448, https://doi.org/10.1093/gji/ggu467

Hammond, J.O.S., J. Wookey, S. Kaneshima, H. Inoue, T. Yamashina and P. Harjadi (2010). Systematic variation in anisotropy beneath the mantle wedge in the Java-Sumatra subduction system from shear-wave splitting, Phys. Earth Planet. Inter., 178, 189-201, https://doi.org/10.1016/j.pepi.2009.10.003

Hatzfeld, D., E. Karagianni, I. Kassaras, A. Kiratzi, E. Louvari, H. Lyon-Caen, K. Makropoulos, P. Papadimitriou, G. Bock and K. Priestley (2001). Shear wave anisotropy in the upper mantle beneath the Aegean related to internal deformation, J. Geophys. Res., 106, 30737, https://doi.org/10.1029/2001JB000387

Hatzfeld, D., V. Karakostas, M. Ziazia, I. Kassaras, E. Papadimitriou, K. Makropoulos, N. Voulgaris and C. Papaioannou (2000). Microseismicity and faulting geometry in the Gulf of Corinth (Greece), Geophys. J. Int., 141, 438-456.

Heimann, S., M. Kriegerowski, M. Isken, S. Cesca, S. Daout, F. Grigoli, C. Juretzek, T. Megies, N. Nooshiri, A. Steinberg, H. Sudhaus, H. Vasyura-Bathke, T. Willey and T. Dahm (2017). Pyrocko - An open-source seismology toolbox and library, https://doi.org/10.5880/GFZ.2.1.2017.001

Hubert, A., G. King, R. Armijo, B. Meyer, B. and D. Papanastasiou (1996). Fault re-activation, stress interaction and rupture propagation of the 1981 Corinth earthquake sequence, Earth Planet. Sci. Lett. 142, 573-585. https://doi.org/10.1016/0012-821X(96)00108-2

Hunter, J.D. (2007). Matplotlib: A 2D Graphics Environment, Comput. Sci. Eng., 9, 90-95, https://doi.org/10.1109/MCSE.2007.55

IGME (Institute of Geology and Mineral Exploration) (1984). Geological map of Greece, Perachora sheet, scale 1:50,000.

Jackson, J. A., J. Gagnepain, G. Houseman, G. C. P. King, P. Papadimitriou, C. Soufleris, J. Virieux (1982). Seismicity, normal faulting, and the geomorphological development of the Gulf of Corinth (Greece): the Corinth earthquakes of February and March 1981, Earth Planet. Sci. Lett., 57, 377-397, https://doi.org/10.1016/0012-821X(82)90158-3

Johnson, J. H., M.K. Savage and J. Townend (2011). Distinguishing between stress-induced and structural anisotropy at Mount Ruapehu volcano, New Zealand, J. Geophys. Res., 116, 12, 1-18, https://doi.org/10.1029/2011JB008308

Johnson, J. H. and M. K. Savage (2012). Tracking volcanic and geothermal activity in the Tongariro Volcanic Centre, New Zealand, with shear wave splitting tomography, J. Volcanol. Geotherm. Res., 223-224, 1-10, https://doi.org/10.1016/j.jvolgeores.2012.01.017

Kaneshima, S., M. Ando and S. Kimura (1988). Evidence from shear-wave splitting for the restriction of seismic anisotropy to the upper crust, Nature, https://doi.org/10.1038/335627a0

Kapetanidis, V. and I. Kassaras (2019). Contemporary crustal stress of the Greek region deduced from earthquake focal mechanisms, J. Geodyn., 123, 55-82, https://doi.org/10.1016/j.jog.2018.11.004

Kapetanidis, V., G. Michas, G. Kaviris and F. Vallianatos (2021). Spatiotemporal Properties of Seismicity and Variations of Shear-Wave Splitting Parameters in the Western Gulf of Corinth (Greece), Appl. Sci., 11, 6573, https://doi.org/10.3390/APP11146573

Karlowska, E., I. D. Bastow, S. Rondenay, R. Martin-Short and R. M. Allen (2021). The development of seismic anisotropy below south-central Alaska: evidence from local earthquake shear wave splitting, Geophys. J. Int., 225, 548-554, https://doi.org/10.1093/GJI/GGAA603

Kassaras, I., V. Kapetanidis, A. Ganas, A. Tzanis, C. Kosma, A. Karakonstantis, S. Valkaniotis., S. Chailas, V. Kouskouna and P. Papadimitriou (2020). The new seismotectonic Atlas of Greece (V1.0) and its implementation, Geosciences, https://doi.org/10.3390/geosciences10110447

Kaviris, G. (2003). Study of seismic source properties of the eastern Gulf of Corinth, PhD Dissertation, National and Kapodistrian University of Athens.

Kaviris, G., V. Kapetanidis, P. Kravvariti, A. Karakonstantis, G. Bozionelos, P. Papadimitriou, N. Voulgaris and K. Makropoulos (2014). Anisotropy Study in Villia (E. Corinth Gulf, Greece), in: 2nd European Conference on Earthquake Engineering and Seismology. Istanbul.

Kaviris, G., I. Fountoulakis, I. Spingos, C. Millas and P. Papadimitriou (2018a). Mantle dynamics beneath Greece from SKS and PKS seismic anisotropy study, Acta Geophys., https://doi.org/10.1007/s11600-018-0225-z

Kaviris, G., C. Millas, I. Spingos, V. Kapetanidis, I. Fountoulakis, P. Papadimitriou, N. Voulgaris and K. Makropoulos (2018b). Observations of shear-wave splitting parameters in the Western Gulf of Corinth focusing on the 2014 $M_w = 5.0$ earthquake, Phys. Earth Planet. Inter., 282, 60-76, https://doi.org/10.1016/j.pepi.2018.07.005

Kaviris, G., I. Spingos, V. Kapetanidis, P. Papadimitriou, and N. Voulgaris (2021). On the origin of upper crustal shear-wave anisotropy at Samos Island, Greece, Acta Geophys., 69, 1051-1064, https://doi.org/10.1007/s11600-021-00598-2

Kaviris, G., I. Spingos, V. Kapetanidis, P. Papadimitriou, N. Voulgaris and K. Makropoulos (2017). Upper crust seismic anisotropy study and temporal variations of shear-wave splitting parameters in the western Gulf of Corinth (Greece) during 2013, Phys. Earth Planet. Inter., 269, 148-164, https://doi.org/10.1016/j.pepi.2017.06.006

Kaviris, G., I. Spingos, V. Karakostas, E. Papadimitriou and T. Tsapanos (2020). Shear-wave splitting properties of the upper crust, during the 2013-2014 seismic crisis, in the CO_2-rich field of Florina Basin, Greece, Phys. Earth Planet. Inter., 303, 106503, https://doi.org/10.1016/j.pepi.2020.106503

Kaviris, G., I. Spingos, C. Millas, V. Kapetanidis, I. Fountoulakis, P. Papadimitriou, N. Voulgaris and G. Drakatos (2018c). Effects of the January 2018 seismic sequence on shear-wave splitting in the upper crust of Marathon (NE Attica, Greece), Phys. Earth Planet. Inter., 285, 45-58, https://doi.org/10.1016/j.pepi.2018.10.007

Kim, J. and Y. Kim (2022). Spatiotemporal variation in upper crustal seismic anisotropy and VP/VS ratio in Groningen gas field, Netherlands: Insights from shear wave splitting, Geophys. J. Int., 232, 1066-1082, https://doi.org/10.1093/GJI/GGAC370

Kranz, R.L. (1983). Microcracks in rocks: A review, Tectonophysics, 100, 449-480, https://doi.org/10.1016/0040-1951(83)90198-1

Krischer, L., T. Megies, R. Barsch, M. Beyreuther, T. Lecocq, C. Caudron and J. Wassermann (2015). ObsPy: A bridge for seismology into the scientific Python ecosystem, Comput. Sci. Discov. 8, 0-17, https://doi.org/10.1088/1749-4699/8/1/014003

Li, Z., Z. Peng, Y. Ben-Zion and F. L. Vernon (2015). Spatial variations of shear wave anisotropy near the San Jacinto Fault Zone in Southern California, J. Geophys. Res. Solid Earth, 120, 8334- 8347 https://doi.org/10.1002/2015JB012483

Li, Z. and Z. Peng (2017). Stress- and Structure-Induced Anisotropy in Southern California From Two Decades of Shear Wave Splitting Measurements, Geophys. Res. Lett, 44, 9607-9614, https://doi.org/10.1002/2017GL075163

Liu, S., S. Crampin, R. Luckett and J. Yang (2014). Changes in shear wave splitting before the 2010 Eyjafjallajökull eruption in Iceland, Geophys. J. Int., 116, 102-112, https://doi.org/10.1093/gji/ggu202

Liu, Y., H. Zhang, C. Thurber and S. Roecker (2008). Shear wave anisotropy in the crust around the San Andreas fault near Parkfield: Spatial and temporal analysis, Geophys. J. Int., 172, 957-970, https://doi.org/10.1111/j.1365-246X.2007.03618.x

Makropoulos, K., G. Kaviris and V. Kouskouna (2012). An updated and extended earthquake catalogue for Greece and adjacent areas since 1900, Nat. Hazards Earth Syst. Sci., 12, 1425-1430, https://doi.org/10.5194/nhess-12-1425-2012

Marriner, N. and C. Morhange (2007). Geoscience of ancient Mediterranean harbours, Earth-Science Rev., 80, 137-194, https://doi.org/10.1016/j.earscirev.2006.10.003

Mechernich, S., S. Schneiderwind, J. Mason, I. D. Papanikolaou, G. Deligiannakis, A. Pallikarakis, S. A. Binnie, T. J. Dunai and K. Reicherter (2018). The Seismic History of the Pisia Fault (Eastern Corinth Rift, Greece) From

Fault Plane Weathering Features and Cosmogenic 36Cl Dating, J. Geophys. Res. Solid Earth, 123, 4266-4284, https://doi.org/10.1029/2017JB014600

Mesimeri, M, V. Karakostas, E. Papadimitriou, G. Tsaklidis and K. Jacobs (2018). Relocation of recent seismicity and seismotectonic properties in the Gulf of Corinth (Greece), Geophys. J. Int., 212, 1123-1142, https://doi.org/10.1093/GJI/GGX450

Michas, G., F. Vallianatos and P. Sammonds (2015). Statistical mechanics and scaling of fault populations with increasing strain in the Corinth Rift, Earth Planet. Sci. Lett., 431, 150-163, https://doi.org/10.1016/J.EPSL.2015.09.014

Michas, G., V. Kapetanidis, I. Spingos, G. Kaviris and F. Vallianatos (2022). The 2020 Perachora peninsula earthquake sequence (East Corinth Rift, Greece): spatiotemporal evolution and implications for the triggering mechanism, Acta Geophys., 70, 2581-2601, https://doi.org/10.1007/S11600-022-00864-X

National Observatory of Athens, Institute of Geodynamics, Athens. (1975). National Observatory of Athens Seismic Network [Data set]. International Federation of Digital Seismograph Networks, https://doi.org/10.7914/SN/HL

Nolte, K.A., G.P. Tsoflias, T.S. Bidgoli and W.L. Watney (2017). Shear-wave anisotropy reveals pore fluid pressure-induced seismicity in the U.S. midcontinent, Sci. Adv., 3, e1700443, https://doi.org/10.1126/sciadv.1700443

Nuttli, O. (1961). The effect of the earth's surface on the S wave particle motion, Bull. Seismol. Soc. Am., 51, 237-246, https://doi.org/10.1785/BSSA0510020237

Ortega-Romo, A. D., J. I. Walter, X. Chen and B.M. Carpenter (2021). Spatially Distinct Tectonic Zones across Oklahoma Inferred from Shear-Wave Splitting, Seis. Res. Lett., 92, 4, 2551-2561, https://doi.org/10.1785/0220200237

Padhy, S. and S. Crampin (2006). High pore-fluid pressures at Bhuj, inferred from 90°-flips in shear-wave polarizations, Geophys. J. Int., 164, 370-376, https://doi.org/10.1111/J.1365-246X.2006.02854.X/2/164-2-370-FIG004.JPEG

Papadimitriou, P., G. Kaviris and K. Makropoulos (1999). Evidence of shear-wave splitting in the eastern Corinthian Gulf (Greece), Phys. Earth Planet. Inter., 114, 3-13.

Papanastassiou, D. (2002). Destructive Earthquakes and Seismotectonics in the Gulf of Corinth, Central Greece: A Review, Springer, Dordrecht, 153-173, https://doi.org/10.1007/978-94-010-0383-4_12

Papazachos, B. C., P. E. Comninakis, E. Papadimitriou and E. M. Scordilis (1984). Properties of the February-March 1981 seismic sequence in the Alkyonides gulf of central Greece, Ann. Geophys., 2, 537-544, https://doi.org/10.1007/BF00879574

Pastori, M., P. Baccheschi and L. Margheriti (2019). Shear Wave Splitting Evidence and Relations With Stress Field and Major Faults From the "Amatrice-Visso-Norcia Seismic Sequence", Tectonics, 38, 3351-3372, https://doi.org/10.1029/2018TC005478

Paulssen, H. (2004). Crustal anisotropy in southern California from local earthquake data, Geophys. Res. Lett., 31, 1601, https://doi.org/10.1029/2003GL018654

Peacock, S., S. Crampin, D. C. Booth and J. B. Fletcher (1988). Shear wave splitting in the Anza Seismic Gap, southern california: Temporal Variations as possible precursors, J. Geophys. Res., 93, 3339-3356, https://doi.org/10.1029/JB093iB04p03339

Peng, Z. and Y. Ben-Zion (2004). Systematic analysis of crustal anisotropy along the Karadere-Düzce branch of the North Anatolian fault, Geophys. J. Int., 159, 253-274, https://doi.org/10.1111/j.1365-246X.2004.02379.x

Polat, G., N. M. Ozel, S. Crampin, S. Ergintav and O. Tan (2012). Shear wave splitting as a proxy for stress forecast of the case of the 2006 Manyas-Kus Golu ($M_b = 5.3$) earthquake, Nat. Hazards Earth Syst. Sci., 12, 1073-1084, https://doi.org/10.5194/nhess-12-1073-2012

Roberts, G.P. and I. Koukouvelas (1996). Structural and seismological segmentation of the Gulf of Corinth fault system: implications for models of fault growth, Ann. Geophys., 39, 3, https://doi.org/10.4401/ag-3996

Sachpazi, M., C. Clément, M. Laigle, A. Hirn and N. Roussos (2003). Rift structure, evolution, and earthquakes in the Gulf of Corinth, from reflection seismic images, Earth Planet. Sci. Lett., 216, 243-257, https://doi.org/10.1016/S0012-821X(03)00503-X

Savage, M.K., Y. Aoki, K. Unglert, T. Ohkura, K. Umakoshi, H. Shimizu, M. Iguchi, T. Tameguri, T. Ohminato and J. Mori (2016). Stress, strain rate and anisotropy in Kyushu, Japan, Earth Planet. Sci. Lett., 439, 129-142, https://doi.org/10.1016/J.EPSL.2016.01.005

Savage, M.K. and P. G. Silver (1993). Mantle deformation and tectonics: constraints from seismic anisotropy in the western United States, Phys. Earth Planet. Inter., 78, 207-227, https://doi.org/10.1016/0031-9201(93)90156-4

Savage, M.K., A. Wessel, N. A. Teanby and A. W. Hurst (2010). Automatic measurement of shear wave splitting and applications to time varying anisotropy at Mount Ruapehu volcano, New Zealand, J. Geophys. Res. Solid Earth, 115, https://doi.org/10.1029/2010JB007722

Schaff, D.P. and P.G. Richards (2014). Improvements in magnitude precision, using the statistics of relative amplitudes measured by cross correlation, Geophys. J. Int., 197, 335-350, https://doi.org/10.1093/gji/ggt433

Seher, T. and I. G. Main (2004). A statistical evaluation of a "stress-forecast" earthquake, Geophys. J. Int., 157, 187-193, https://doi.org/10.1111/j.1365-246X.2004.02186.x

Sharma, A., S. Baruah, D. Piccinini, S. Saikia, M. K. Phukan, M. Chetia and J. R. Kayal (2017). Crustal seismic anisotropy beneath Shillong plateau - Assam valley in North East India: Shear-wave splitting analysis using local earthquakes, Tectonophysics, 717, 425-432, https://doi.org/10.1016/j.tecto.2017.08.027

Shi, Y., Y. Gao, X. Shen and K. H. Liu (2020). Multiscale spatial distribution of crustal seismic anisotropy beneath the northeastern margin of the Tibetan plateau and tectonic implications of the Haiyuan fault, Tectonophysics, 774, 228274, https://doi.org/10.1016/j.tecto.2019.228274

Silver, P. G. and W. W. Chan (1991). Shear Wave Splitting and Sub continental Mantle Deformation, J. Geophys. Res., 96, 429-454, https://doi.org/10.1029/91JB00899

Spingos, I., G. Kaviris, C. Millas, P. Papadimitriou and N. Voulgaris (2020). Pytheas: An open-source software solution for local shear-wave splitting studies, Comput. Geosci., 134, 104346, https://doi.org/10.1016/j.cageo.2019.104346

Stucchi, M., A. Rovida, A. A. Gomez Capera, P. Alexandre, T. Camelbeeck, M. B. Demircioglu, P. Gasperini, V. Kouskouna, R. M. W. Musson, M. Radulian, K. Sesetyan, S. Vilanova, D. Baumont, H. Bungum, D. Fäh, W. Lenhardt, K. Makropoulos, J. M. Martinez Solares, O. Scotti, M. Živčić, P. Albini, J. Batllo, C. Papaioannou, R. Tatevossian, M. Locati, C. Meletti, D. Viganò, D. Giardini (2013). The SHARE European Earthquake Catalogue (SHEEC) 1000-1899, J. Seismol., 17, 523-544, https://doi.org/10.1007/s10950-012-9335-2

Taymaz, T., J. Jackson and D.P. Mckenzie (1991). Active tectonics of the north and central Aegean Sea. Geophys. J. Int., 106, 433-490, https://doi.org/10.1111/j.1365-246X.1991.tb03906.x

Teanby, N., J. M. Kendall and M. van der Baan (2004). Automation of shear-wave splitting measurements using cluster analysis, Bull. Seismol. Soc. Am., 94, 453-463, https://doi.org/10.1785/0120030123

Tillotson, P., J. Sothcott, A. I. Best, M. Chapman and X. Y. Li (2012). Experimental verification of the fracture density and shear-wave splitting relationship using synthetic silica cemented sandstones with a controlled fracture geometry, Geophys. Prospect., 60, 516-525, https://doi.org/10.1111/J.1365-2478.2011.01021.X

Uieda, L., D. Tian, W. J. Leong, L. Toney, W. Schlitzer, J. Yao, M. Grund, M. Jones, K. Materna, T. Newton, M. Ziebarth and P. Wessel (2021). PyGMT: A Python interface for the Generic Mapping Tools, https://doi.org/10.5281/ZENODO.4592991

University of Athens. (2008). Hellenic Seismological Network, University of Athens, Seismological Laboratory [Data set]. International Federation of Digital Seismograph Networks, https://doi.org/10.7914/SN/HA

University of Patras. (2000). University of Patras, Seismological Laboratory [Data set]. International Federation of Digital Seismograph Networks, https://doi.org/10.7914/SN/HP

Valcke, S.L.A., M. Casey, G. E. Lloyd, J. M. Kendall and Q. J. Fisher (2006). Lattice preferred orientation and seismic anisotropy in sedimentary rocks, Geophys. J. Int., 166, 652-666, https://doi.org/10.1111/j.1365-246X.2006.02987.x

Vita-Finzi, C. and G. C. P. King, (1985). The Seismicity, Geomorphology and Structural Evolution of the Corinth Area of Greece, Philos. Trans. R. Soc. A Math. Phys. Eng. Sci., 314, 379-407, https://doi.org/10.1098/rsta.1985.0024

Walsh, E., R. Arnold and M. K. Savage (2013). Silver and Chan revisited, J. Geophys. Res. Solid Earth, 118, 5500-5515, https://doi.org/10.1002/jgrb.50386

Wessel, P., J. F. Luis, L. Uieda, R. Scharroo, F. Wobbe, W. H. F. Smith and D. Tian (2019). The Generic Mapping Tools Version 6, Geochemistry, Geophys. Geosystems, 20, 5556-5564, https://doi.org/10.1029/2019GC008515

Wuestefeld, A., J. M. Kendall, J. P. Verdon and A. Van As (2011). In situ monitoring of rock fracturing using shear wave splitting analysis: An example from a mining setting, Geophys. J. Int., 187, 848-860. https://doi.org/10.1111/j.1365-246X.2011.05171.x

Wüstefeld, A. and G. Bokelmann (2007). Null detection in shear-wave splitting measurements, Bull. Seismol. Soc. Am., 97, 1204-1211, https://doi.org/10.1785/0120060190

Zatsepin, S. and S. Crampin, S. (1997). Modelling the compliance of crustal rock—I. Response of shear-wave splitting to differential stress, Geophys. J. Int., 129, 477-494, https://doi.org/10.1111/j.1365-246X.1997.tb04488.x

Zhang, B., S. Zhang, T. Wu and Y. Hua (2018). Upper crustal anisotropy from local shear-wave splitting and crust-mantle coupling of Yunnan, SE margin of Tibetan Plateau, Geod. Geodyn., 9, 302-311, https://doi.org/10.1016/j.geog.2018.01.004

Zhu, W. and G. C. Beroza (2019). PhaseNet: a deep-neural-network-based seismic arrival-time picking method, Geophys. J. Int., 216, 261-273, https://doi.org/10.1093/gji/ggy423

***CORRESPONDING AUTHOR: Ioannis SPINGOS**,
Section of Geophysics – Geothermics, Department of Geology and Geoenvironment, National and Kapodistrian University of Athens, Athens, Greece
e-mail: ispingos@geol.uoa.gr